

VERIFICATION OF NUMERICAL MODELS FOR SEISMIC FLUID-STRUCTURE-INTERACTION ANALYSIS OF INTERNAL COMPONENTS IN LIQUID-FILLED ADVANCED REACTORS

Ching-Ching Yu^{1*} and Andrew S. Whittaker²

¹Ph.D. Candidate, Department of Civil, Structural, and Environmental Engineering, University at Buffalo, Buffalo, NY 14260, USA (cyu23@buffalo.edu)

²SUNY Distinguished Professor, Department of Civil, Structural, and Environmental Engineering, University at Buffalo, Buffalo, NY 14260, USA (awhittak@buffalo.edu)

*Corresponding Author

Earthquake shaking of a liquid-filled advanced reactor induces fluid-structure interaction (FSI) between the reactor vessel (tank), its internal components, and the contained liquid. Seismic design, qualification, and risk assessment of such reactors must consider fluid-structure responses, their geometries and support conditions, and three-directional seismic inputs, all of which require numerical simulations. Numerical models used for analysis of safety-related nuclear equipment must be verified and validated. This paper verifies numerical models of submerged components using analytical solutions. Seismic FSI analysis of the numerical models are performed using the Arbitrary Lagrangian-Eulerian and Incompressible Computational Fluid Dynamics solvers in LS-DYNA. Prior analytical solutions are re-worked in this paper, and calculation errors are identified and corrected. The solutions address frequencies of two concentric cylindrical pipes filled with liquid: the inner pipe is a submerged component, and the outer pipe contains the liquid. A unitless frequency coefficient is defined and presented for pipes of different materials, filled with different liquids, and with a range of dimensions, for application to advanced reactors. The numerical models are verified here by comparing the lateral frequencies of submerged components with those calculated using the corrected analytical solutions. Recommendations for verification of numerical models of internal components in advanced reactors for seismic FSI analysis are provided. Although the unitless frequency coefficients and verification procedures are developed for application to advanced nuclear reactors, they are broadly applicable to FSI analysis of submerged components in liquid-filled vessels such as storage tanks, boilers, and steam generators.

KEYWORDS

Seismic fluid-structure interaction, submerged components, verification of numerical models, advanced nuclear reactors, ARPA-E

1. INTRODUCTION

Fluid-structure interaction (FSI) analysis is required for the seismic design of submerged equipment in many engineering applications: liquid storage tanks, boilers, process equipment, and reactors, steam generators, and spent fuel pools in nuclear power plants.

A liquid-filled advanced nuclear reactor includes a vessel and internal components immersed or submerged in the contained liquid coolant. Figure 1¹ presents an example: a prototype liquid sodium reactor. (The colored lines in Figure 1 are used to identify the dimensions of the internal components described in Section 2.2.) The seismic design, qualification, and risk assessment of such an advanced reactor must consider the interaction between the vessel, its internal components, and the liquid, their specific geometries and support conditions, and three (translational) to six (translational and rotational) components of earthquake shaking, none of which can be accommodated by analytical solutions. Numerical analysis is the only viable pathway for design of these submerged components because analytical solutions are very limited in terms of geometry, boundary conditions and seismic inputs, and full-scale testing is physically impractical, time consuming, and expensive.

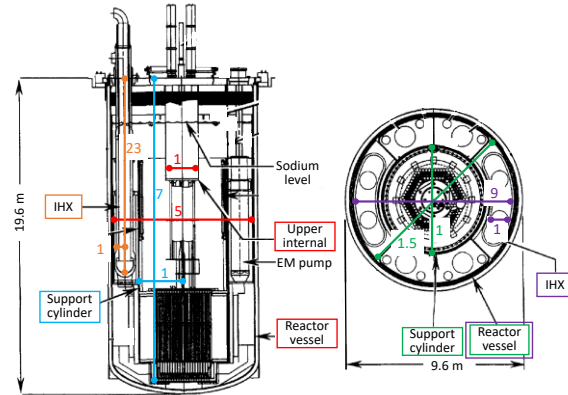


Figure 1. Prototype advanced reactor ¹, including a reactor vessel, internal components, and contained liquid sodium; orange and blue lines indicating the height-to-radius ratios H / R_1 for the internal components; red, green, and purple lines indicating the radius ratios R_2 / R_1 for the internal components to the reactor vessel

Numerical models used for analysis, design, qualification, and risk assessment of safety-related nuclear equipment are required to be verified and validated, which is unique to the nuclear sector. Numerical models can be verified by comparing predictions with analytical solutions and then validated using experimental data. Prior analytical work on FSI has not considered nonlinear fluid responses and coupling of responses in different directions, and so verification of numerical models utilizes solutions for unidirectional shaking of a small amplitude. Validation of a verified model would consider nonlinear fluid responses to multi-directional intense shaking generated from experiments. To the knowledge of the authors, none of the analytical studies for FSI of a vessel (tank) that address all responses critical to seismic design (e.g., pressures on the tank and internal components, reactions at their supports, and wave heights of the contained liquid) consider interaction with internal components. Consequently, verification studies would have to be performed separately for models of: 1) fluid-structure responses of a vessel (excluding the internal components), and 2) frequencies and/or interaction responses of internal components in the vessel. Yu and Whittaker² verified numerical models for tanks (excluding internal components) by comparing results of fluid-structure responses considered in seismic design with those calculated using analytical solutions³⁻⁵. These verified models were validated using test data generated from earthquake-simulator experiments of a water-filled tank^{2, 6, 7}, and challenges associated with generating reliable numerical simulations of nonlinear fluid-structure responses (e.g., sloshing) were identified. Herein, numerical models of components submerged in a liquid-filled vessel are verified for small-amplitude, unidirectional, horizontal motion. Data from earthquake-simulator testing of a liquid-filled tank equipped with central and off-center components⁸⁻¹⁰ will be used for validation studies and reported elsewhere.

If the internal components of Figure 1 displace laterally due to horizontal seismic motion, the adjacent liquid generates hydrodynamic pressures (loadings) on their surfaces. If the amplitude of the input is small, the adjacent liquid is attached to and moves with the components, which reduces their frequencies: the so-called added mass effect. Analytical solutions were derived to address hydrodynamic loadings on and frequencies of submerged cylindrical rods and pipes for application to nuclear reactors¹¹⁻¹⁶ and referenced in ASCE/SEI Standard 4¹⁷. (Components in nuclear reactors are generally cylindrical structures: the upper internal, intermediate heat exchanger (IHX), and electromagnetic (EM) pump in Figure 1 for example.) Analytical solutions for frequencies of two concentric cylindrical pipes filled with liquid are used here to verify numerical models. The inner pipe is a central internal component (e.g., the upper internal in Figure 1), and the outer pipe is the wall of the reactor vessel. The analytical solutions derived by Chen and Rosenberg¹⁵ are re-worked and corrected. Numerical models are developed for two liquid-filled concentric pipes, and the analysis results are compared with those calculated using the corrected analytical solutions. The Arbitrary Lagrangian-Eulerian (ALE) and Incompressible Computational Fluid Dynamics (ICFD) solvers in LS-DYNA¹⁸ are used for the numerical analysis. Both solvers are capable of nonlinear FSI calculations.

Section 2 presents the derivation and results of the analytical solutions for lateral frequencies of liquid-filled concentric pipes, derived by Chen and Rosenberg¹⁵ and corrected in this paper. Section 3 presents the development and verification of ALE and ICFD models. Section 4 presents a summary and conclusions of the verification study, and provides recommendations for verifying a numerical model for seismic FSI analysis of submerged components in a reactor vessel.

2. ANALYTICAL SOLUTIONS

Fritz¹⁶ derived analytical solutions for added masses for a solid cylinder submerged in a fluid confined by a pipe container. Fritz assumed the solid cylinder and the pipe to be rigid and so did not solve for lateral frequencies.

Chen and Rosenberg¹⁵ derived analytical solutions for frequencies of two liquid (fluid)-filled concentric pipes shown in Figure 2, with identical lengths and boundary conditions. The pipes were assumed to be either elastic or rigid with a constant thickness. The fluid was assumed to be inviscid, and compressibility was considered. The pipes were assumed to be filled fully: there was no free surface. Atmospheric and hydrostatic pressures were not taken into account. The analytical solutions were derived for the frequencies of lateral, circumferential, axial, and torsional motions of the pipes.

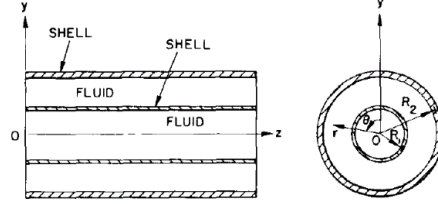


Figure 2. Two concentric cylindrical pipes filled with fluid¹⁵

Chen and Rosenberg's analytical solutions¹⁵ are re-derived and corrected as needed. Mistakes made in their derivation are identified and quantified. The fluid is assumed to be incompressible, which is reasonable for the liquid in many nuclear reactors: sodium-cooled, boiling-water, and pressurized-water reactors. The frequencies of the fluid-filled pipes associated with lateral motions are discussed. (Based on the orientation of the vessel and central components of Figure 1, the pipes are vertical and the seismic input that generates lateral motions is horizontal.) A unitless frequency coefficient is defined using the corrected solutions and presented for pipes of different materials, filled with different fluids, and with a range of dimensions practical to advanced reactors. The lateral frequencies of pipes are calculated using the corrected analytical solutions and the unitless frequency coefficient.

2.1 Derivation

Figure 3a presents concentric pipes in two cutaway views and introduces the variables used in the derivation for the analytical solutions, a Cartesian coordinate system (x, y, z) , and a cylindrical coordinate system (z, θ, r) . In the figure, "Pipe 1" refers to the inner pipe, "Pipe 2" refers to the outer pipe, "Fluid 1" refers to the liquid filling the inner pipe, and "Fluid 2" refers to the liquid filling the annulus between the two pipes. This numbering system is consistent with the subscripts of the variables using in the derivation here and those of Chen and Rosenberg¹⁵. For the inner (outer) pipe, the radius, height, and wall thickness are R_1 , H_1 , and h_1 (R_2 , H_2 , and h_2), respectively. The heights of the two pipes are identical: $H_1 = H_2 = H$. The axial (z), tangential (θ), and radial (r) displacements on the wall of the inner pipe are u_{s1} , v_{s1} , and w_{s1} , respectively, and the counterparts for the outer pipe are u_{s2} , v_{s2} , and w_{s2} . The radial (r) velocity of the fluid inside the inner pipe is V_1 , and that in the annulus is V_2 .

Chen and Rosenberg¹⁵ used the equilibrium equations for cylindrical shells provided by Flugge¹⁹ to relate the displacements of the pipes to their inertial forces and hydrodynamic loadings. Flugge equilibrated the stresses of and external forces on a unit area of a cylindrical shell using three differential equations (Eq. (13a-c) on page 219 in Flugge):

$$\left[\frac{\partial^2}{\partial z^2} + \frac{1-\nu}{2R^2} \left(1 + \frac{h^2}{12R^2} \right) \frac{\partial^2}{\partial \theta^2} \right] u_s + \frac{1+\nu}{2R} \frac{\partial^2}{\partial z \partial \theta} v_s + \left[\frac{\nu}{R} \frac{\partial}{\partial z} - \frac{h^2}{12R} \frac{\partial^3}{\partial z^3} + \frac{(1-\nu)h^2}{24R^3} \frac{\partial^3}{\partial z \partial \theta^2} \right] w_s = F_u \frac{1-\nu^2}{Eh} \quad (1)$$

$$\frac{1+\nu}{2R} \frac{\partial^2}{\partial z \partial \theta} u_s + \left[\frac{1}{R} \frac{\partial^2}{\partial \theta^2} + \frac{1-\nu}{2} \left(1 + \frac{h^2}{4R^2} \right) \frac{\partial^2}{\partial z^2} \right] v_s + \left[\frac{1}{R^2} \frac{\partial}{\partial \theta} - \frac{(3-\nu)h^2}{24R^2} \frac{\partial^3}{\partial z^2 \partial \theta} \right] w_s = F_v \frac{1-\nu^2}{Eh} \quad (2)$$

$$\left[-\frac{h^2}{12R} \frac{\partial^3}{\partial z^3} + \frac{\nu}{R} \frac{\partial}{\partial z} + \frac{(1-\nu)h^2}{24R^3} \frac{\partial^3}{\partial z \partial \theta^2} \right] u_s + \left[-\frac{(3-\nu)h^2}{24R^2} \frac{\partial^3}{\partial z^2 \partial \theta} + \frac{1}{R^2} \frac{\partial}{\partial \theta} \right] v_s + \left[\frac{1}{R^2} + \frac{1}{12R^4} + \frac{1}{12} \frac{\partial^4}{\partial z^4} + \frac{h^2}{6R^2} \frac{\partial^2}{\partial z^2 \partial \theta^2} + \frac{h^2}{12R^4} \frac{\partial^4}{\partial \theta^4} + \frac{h^2}{6R^4} \frac{\partial^2}{\partial \theta^2} \right] w_s = -F_w \frac{1-\nu^2}{Eh} \quad (3)$$

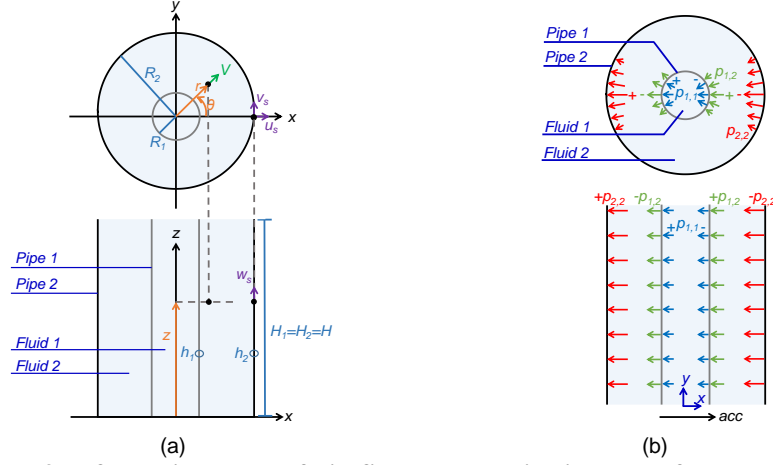


Figure 3. Information on two fluid-filled concentric pipes used for the analytical solutions: (a) variables and coordinate systems; (b) hydrodynamic pressures on the pipes accelerating in the x direction

where E , ν , R , and h are the elastic modulus, Poisson's ratio, radius, and wall thickness of the cylindrical shell; u_s , v_s , and w_s are the displacements of the shell along the z , θ , and r coordinates, respectively; and F_u , F_v , and F_w are the forces per unit area on the shell along the respective coordinates. Chen and Rosenberg¹⁵ applied Eqs. (1) to (3) to the pipes of Figure 3a. For the inner pipe, a subscript "1" was added to each of the variables used in the three equations: E_1 , ν_1 , R_1 , h_1 , u_{s1} , v_{s1} , w_{s1} , F_{u1} , F_{v1} , and F_{w1} . The corresponding variables for the outer pipe were E_2 , ν_2 , R_2 , h_2 , u_{s2} , v_{s2} , w_{s2} , F_{u2} , F_{v2} , and F_{w2} .

The displacements on the walls of the two pipes were assumed to be:

$$u_{sj}(t, z, \theta) = \bar{u}_{sj} \cdot \cos \theta \cdot e^{i(\omega t - \frac{2\pi z}{l})} \quad (4)$$

$$v_{sj}(t, z, \theta) = \bar{v}_{sj} \cdot \sin \theta \cdot e^{i(\omega t - \frac{2\pi z}{l})} \quad (5)$$

$$w_{sj}(t, z, \theta) = \bar{w}_{sj} \cdot \cos \theta \cdot e^{i(\omega t - \frac{2\pi z}{l})} \quad (6)$$

where $j = 1$ and 2 , referring to inner and outer pipes, respectively; \bar{u}_{sj} , \bar{v}_{sj} , and \bar{w}_{sj} are coefficients for the displacements; ω and l are the angular frequency and the wavelength of the pipes in a given eigen mode. (Note that a wavelength l represents the shape in a given lateral mode of an elastic beam with a uniform cross section. The wavelength of a beam is smaller in a higher lateral mode. Values of l were derived for beams with different boundary conditions²⁰: l are $3.35H$ and $1.34H$ for the first two modes of a cantilever and those for a simply-supported beam are $2H$ and H . See Figure 2 of the digital appendix²¹ for more information.)

The forces (per unit area) on the pipes included inertial forces and hydrodynamic pressures. The inertial forces were associated with the accelerations of the pipes along the three axes, z , θ , and r . The hydrodynamic pressures were normal to the walls of the pipes, namely in the r direction, and so were included in F_{w1} and F_{w2} :

$$F_{uj} = -\rho_{sj} h_j \cdot u_{sj}'' \quad (7)$$

$$F_{vj} = -\rho_{sj} h_j \cdot v_{sj}'' \quad (8)$$

$$F_{w1} = -\rho_{s1} h_1 \cdot w_{s1}'' + p_{1,1} - p_{1,2} \quad (9)$$

$$F_{w2} = -\rho_{s2} h_2 \cdot w_{s2}'' + p_{2,2} \quad (10)$$

where $j = 1$ and 2 ; ρ_{s1} and ρ_{s2} are the densities of the material of the pipes; and $p_{1,1}$, $p_{1,2}$, and $p_{2,2}$ are hydrodynamic pressures on the pipes, as shown in Figure 3b. The two pipes in the figure accelerate in the x direction, and $p_{1,1}$ is the hydrodynamic pressure on the inner surface of the inner pipe (generated by Fluid 1), $p_{1,2}$ is that on the outer surface of the inner pipe (generated by Fluid 2), and $p_{2,2}$ is that on the inner surface of the outer pipe (generated by Fluid 2). The pressure, p , and the velocity, vel , of the fluid were described using its velocity potential, Φ :

$$p(r, \theta, z) = -\rho \frac{\partial \Phi}{\partial t} \quad (11)$$

$$vel(z, \theta, r) = \nabla \Phi = \frac{\partial \Phi}{\partial z} \bar{z} + \frac{1}{r} \frac{\partial \Phi}{\partial \theta} \bar{\theta} + \frac{\partial \Phi}{\partial r} \bar{r} \quad (12)$$

where ρ is the density of the fluid, t is time, and ∇ is the gradient operator with respect to coordinates (z, θ, r). The fluid velocity, vel , includes the vectors of the z, θ , and r components. Both p and vel calculated using Φ are functions of z, θ , and r , which enables the determination of the responses for any locations in the fluid. Given assumed fluid velocities adjacent to the pipes (i.e., boundary conditions), Eqs. (11) and (12) were used by Chen and Rosenberg¹⁵ to derive velocity potentials and calculate fluid pressures. The velocity potentials were assumed to take the form of the radial displacements of the pipes per Eq. (6):

$$\Phi_k = \bar{\Phi}_k(r) \cdot \cos \theta \cdot e^{i(\alpha r - \frac{2\pi z}{l})} \quad (13)$$

where $k = 1$ and 2 , referring to Fluids 1 and 2, respectively; $\bar{\Phi}_k$ is a function of r , to be solved using the boundary conditions. Since Fluids 1 and 2 are assumed to be incompressible here, the divergence of the fluid velocity is zero (i.e., no inlet, outlet, and change in the density; $\nabla \cdot vel = 0$), and so the velocity potential satisfies Laplace's equation: $\nabla \cdot vel = \nabla^2 \Phi_k = 0$ per Eq. (12). Subjected to small-amplitude motions in the x direction, the fluid adjacent to the walls of the pipes (at $r = R_1$ or R_2) was assumed to move at identical velocities:

$$V_1(r = R_1) = \left. \frac{\partial \Phi_1}{\partial r} \right|_{r=R_1} = w'_{s1} \quad (14)$$

$$V_2(r = R_1) = \left. \frac{\partial \Phi_2}{\partial r} \right|_{r=R_1} = w'_{s1} \quad (15)$$

$$V_2(r = R_2) = \left. \frac{\partial \Phi_2}{\partial r} \right|_{r=R_2} = w'_{s2} \quad (16)$$

where V_1 and V_2 are the radial velocities of Fluids 1 and 2, respectively, calculated using Eq. (12), which leads to the second terms of Eqs. (14) to (16); w'_{s1} and w'_{s2} are radial velocities of the inner and outer pipes, respectively. Substituting Eq. (13) to Eqs. (14) to (16) for Φ_1 and Φ_2 , the velocity potentials are calculated:

$$\Phi_1 = \frac{I(\gamma)}{I'(\alpha_1)} i\omega \cdot \bar{w}_{s1} \cdot \cos \theta \cdot e^{i(\alpha r - \frac{2\pi z}{l})} \quad (17)$$

$$\Phi_2 = \left(\frac{I_1(\gamma)K'_1(\alpha_2) - K_1(\gamma)I'_1(\alpha_2)}{I'_1(\alpha_1)K'_1(\alpha_2) - K'_1(\alpha_1)I'_1(\alpha_2)} \bar{w}_{s1} + \frac{K_1(\gamma)I'_1(\alpha_1) - I_1(\gamma)K'_1(\alpha_1)}{I'_1(\alpha_1)K'_1(\alpha_2) - K'_1(\alpha_1)I'_1(\alpha_2)} \bar{w}_{s2} \right) \cos \theta \cdot e^{i(\alpha r - \frac{2\pi z}{l})} \quad (18)$$

where $\alpha_1 = 2\pi R_1 / l$, $\alpha_2 = 2\pi R_2 / l$, and $\gamma = 2\pi r / l$; I_1 and K_1 are the modified Bessel functions of the first and second kind, respectively; I'_1 and K'_1 are the first derivatives of the modified Bessel functions with respect to r (i.e., $I'_1(\gamma) = \frac{2\pi}{l} \frac{\partial I_1(\gamma)}{\partial \gamma}$ and $K'_1(\gamma) = \frac{2\pi}{l} \frac{\partial K_1(\gamma)}{\partial \gamma}$). The hydrodynamic pressure $p_{1,1}$ was calculated per Eq. (11) using Φ_1 of Eq. (17):

$$p_{1,1} = -\rho_1 \left. \frac{\partial \Phi_1}{\partial t} \right|_{r=R_1} = \rho_1 \omega^2 \frac{I_1(\alpha_1)}{I'_1(\alpha_1)} \cdot \bar{w}_{s1} \cdot \cos \theta \cdot e^{i(\alpha r - \frac{2\pi z}{l})} \quad (19)$$

where ρ_1 is the density of Fluid 1. The pressures $p_{1,2}$ and $p_{2,2}$ were calculated per Eq. (11) using Φ_2 of Eq. (18):

$$p_{1,2} = -\rho_2 \left. \frac{\partial \Phi_2}{\partial t} \right|_{r=R_1} = \rho_2 \omega^2 \left(\frac{I_1(\alpha_1)K'_1(\alpha_2) - K_1(\alpha_1)I'_1(\alpha_2)}{I'_1(\alpha_1)K'_1(\alpha_2) - K'_1(\alpha_1)I'_1(\alpha_2)} \bar{w}_{s1} + \frac{K_1(\alpha_1)I'_1(\alpha_1) - I_1(\alpha_1)K'_1(\alpha_1)}{I'_1(\alpha_1)K'_1(\alpha_2) - K'_1(\alpha_1)I'_1(\alpha_2)} \bar{w}_{s2} \right) \cos \theta \cdot e^{i(\alpha r - \frac{2\pi z}{l})} \quad (20)$$

$$p_{2,2} = -\rho_2 \left. \frac{\partial \Phi_2}{\partial t} \right|_{r=R_2} = \rho_2 \omega^2 \left(\frac{I_1(\alpha_2)K'_1(\alpha_2) - K_1(\alpha_2)I'_1(\alpha_2)}{I'_1(\alpha_1)K'_1(\alpha_2) - K'_1(\alpha_1)I'_1(\alpha_2)} \bar{w}_{s1} + \frac{K_1(\alpha_2)I'_1(\alpha_1) - I_1(\alpha_2)K'_1(\alpha_1)}{I'_1(\alpha_1)K'_1(\alpha_2) - K'_1(\alpha_1)I'_1(\alpha_2)} \bar{w}_{s2} \right) \cos \theta \cdot e^{i(\alpha r - \frac{2\pi z}{l})} \quad (21)$$

where ρ_2 is the density of Fluid 2. Equations (20) and (21) include both \bar{w}_{s1} and \bar{w}_{s2} , namely, $p_{1,2}$ and $p_{2,2}$ are associated with the radial displacements of both the inner and outer pipes. Accordingly, the hydrodynamic pressure on each pipe generated by the fluid in the annulus (i.e., $p_{1,2}$ and $p_{2,2}$ by Fluid 2) is affected by the response of the other pipe: Fluid 2 couples the two pipes. (If there is no fluid in the annulus, the responses of the two pipes are independent.)

Given the displacements u_{s1} , v_{s1} , and w_{s1} (Eqs. (4) to (6) with $j = 1$) and the forces F_{u1} , F_{v1} , and F_{w1} (Eqs. (7) to (9) with $j = 1$), Chen and Rosenberg¹⁵ derived three equilibrium equations for the inner pipe using Flugge's equation per Eqs. (1) to (3). Similarly, given u_{s2} , v_{s2} , and w_{s2} per Eqs. (4) to (6) and F_{u2} , F_{v2} , and F_{w2} per Eqs. (7), (8), and (10), with $j = 2$, three equilibrium equations for the outer pipe were yielded. The six equilibrium equations were then reformatted as Eq. (22). The first three rows of $[F]$ in Eq. (22) are associated with the inner pipe and the last three rows are associated with the outer pipe:

$$[F]_{6 \times 6} \cdot \begin{Bmatrix} \bar{u}_{s1} \\ \bar{v}_{s1} \\ \bar{w}_{s1} \\ \bar{u}_{s2} \\ \bar{v}_{s2} \\ \bar{w}_{s2} \end{Bmatrix} = \begin{bmatrix} a_{11} & a_{12} & a_{13} & 0 & 0 & 0 \\ a_{12} & a_{14} & a_{15} & 0 & 0 & 0 \\ a_{13} & a_{15} & a_{16} & 0 & 0 & a_{17} \\ 0 & 0 & 0 & a_{21} & a_{22} & a_{23} \\ 0 & 0 & 0 & a_{22} & a_{24} & a_{25} \\ 0 & 0 & a_{27} & a_{23} & a_{25} & a_{26} \end{bmatrix} \cdot \begin{Bmatrix} \bar{u}_{s1} \\ \bar{v}_{s1} \\ \bar{w}_{s1} \\ \bar{u}_{s2} \\ \bar{v}_{s2} \\ \bar{w}_{s2} \end{Bmatrix} = \begin{bmatrix} F_1 & 0 & 0 & 0 \\ 0 & 0 & 0 & 0 \\ 0 & 0 & 0 & 0 \\ 0 & 0 & 0 & F_2 \\ 0 & 0 & 0 & 0 \\ 0 & 0 & a_{17} & 0 \end{bmatrix} \cdot \begin{Bmatrix} \bar{u}_{s1} \\ \bar{v}_{s1} \\ \bar{w}_{s1} \\ \bar{u}_{s2} \\ \bar{v}_{s2} \\ \bar{w}_{s2} \end{Bmatrix} = 0 \quad (22)$$

The first digit of the subscript of each entry a in $[F]$ is either 1 or 2, indicating the associated equilibrium equations for the inner or outer pipes, respectively. To explain the composition and arrangement of the entries in $[F]$, the matrix is parsed here into two 3×3 submatrices, $[F_1]$ and $[F_2]$, and two nonzero entries, a_{17} and a_{27} . Matrices $[F_1]$ and $[F_2]$ are symmetric. Matrix $[F_1]$ relates the inertial forces on Pipe 1 (inner pipe) to its displacements, u_{s1} , v_{s1} , and w_{s1} , and relates the hydrodynamic pressures, $p_{1,1}$ and $p_{1,2}$, to w_{s1} through a_{16} . All entries in $[F_1]$ are functions of the dimensions and mechanical properties of Pipe 1, and a_{16} further includes dimensions and densities of Fluids 1 and 2. The entries in $[F_1]$ are:

$$a_{11} = -\alpha_1^2 - \frac{1-\nu_1}{2} \left(1 + \frac{h_1^2}{12R_1^2}\right) + \omega^2 \cdot \frac{R_1^2 \rho_{s1} (1-\nu_1^2)}{E_1} \quad (23)$$

$$a_{12} = -i \cdot \alpha_1 \frac{1+\nu_1}{2} \quad (24)$$

$$a_{13} = -i \cdot \left(\nu_1 \alpha_1 + \frac{h_1^2}{12R_1} \left(\alpha_1^3 - \frac{1-\nu_1}{2} \alpha_1 \right) \right) \quad (25)$$

$$a_{14} = 1 + \alpha_1^2 \left(\frac{1-\nu_1}{2} \right) \left(1 + \frac{h_1^2}{4R_1^2} \right) - \omega^2 \cdot \frac{R_1^2 \rho_{s1} (1-\nu_1^2)}{E_1} \quad (26)$$

$$a_{15} = 1 + \frac{h_1^2}{24R_1^2} (3-\nu_1) \alpha_1^2 \quad (27)$$

$$a_{16} = 1 + \frac{h_1^2 (\alpha_1^4 + 2\alpha_1^2)}{12R_1^2} - \frac{\omega^2 R_1^2 \rho_{s1} (1-\nu_1^2)}{E_1} \cdot \left(1 + \frac{\rho_1}{h_1 \rho_{s1}} \frac{I_1(\alpha_1)}{I_1'(\alpha_1)} - \frac{\rho_2}{h_1 \rho_{s1}} \frac{I_1(\alpha_1) K_1'(\alpha_2) - K_1(\alpha_1) I_1'(\alpha_2)}{I_1'(\alpha_1) K_1'(\alpha_2) - K_1'(\alpha_1) I_1'(\alpha_2)} \right) \quad (28)$$

Matrix $[F_2]$ relates the inertial forces on Pipe 2 to its displacements, u_{s2} , v_{s2} , and w_{s2} , and relates $p_{2,2}$ to w_{s2} through a_{26} . All entries in $[F_2]$ are functions of the dimensions and mechanical properties of Pipe 2, and the form of a_{26} further includes the dimensions and density of Fluid 2. Entry a_{26} is:

$$a_{26} = 1 + \frac{h_2^2 (\alpha_2^4 + 2\alpha_2^2)}{12R_2^2} - \frac{\omega^2 R_2^2 \rho_{s2} (1-\nu_2^2)}{E_2} \cdot \left(1 + \frac{\rho_2}{h_2 \rho_{s2}} \frac{K_1(\alpha_2) I_1'(\alpha_1) - I_1(\alpha_2) K_1'(\alpha_1)}{I_1'(\alpha_1) K_1'(\alpha_2) - K_1'(\alpha_1) I_1'(\alpha_2)} \right) \quad (29)$$

Entries a_{21} , a_{22} , a_{23} , a_{24} , and a_{25} in $[F_2]$ are counterparts of a_{11} , a_{12} , a_{13} , a_{14} , and a_{15} in $[F_1]$, respectively, and calculated by replacing the dimensions and mechanical properties of Pipe 1 in Eqs. (23) to (27) with those of Pipe 2: substituting the subscript "1" of each variable with "2".

Entries a_{17} and a_{27} couple the responses of the two pipes due to the presence of Fluid 2 in the annulus. Entry a_{17} relates the hydrodynamic pressure on Pipe 1 to the radial displacement w_{s2} of Pipe 2, which is associated with $p_{1,2}$ per Eq. (20):

$$a_{17} = \frac{\omega^2 R_1^2 \rho_{s1} (1-\nu_1^2)}{E_1} \cdot \frac{\rho_2}{h_1 \rho_{s1}} \frac{K_1(\alpha_1) I_1'(\alpha_1) - I_1(\alpha_1) K_1'(\alpha_1)}{I_1'(\alpha_1) K_1'(\alpha_2) - K_1'(\alpha_1) I_1'(\alpha_2)} \quad (30)$$

Similarly, a_{27} relates the hydrodynamic pressure on Pipe 2 to the radial displacement w_{s1} of Pipe 1, which is associated $p_{2,2}$ per Eq. (21):

$$a_{27} = -\frac{\omega^2 R_2^2 \rho_{s2} (1-\nu_2^2)}{E_2} \cdot \frac{\rho_2}{h_2 \rho_{s2}} \frac{I_1(\alpha_2) K_1'(\alpha_2) - K_1(\alpha_2) I_1'(\alpha_2)}{I_1'(\alpha_1) K_1'(\alpha_2) - K_1'(\alpha_1) I_1'(\alpha_2)} \quad (31)$$

Note that Eqs. (28), (29), (30), and (31), as written by Chen and Rosenberg¹⁵, involved calculation errors. These errors are identified and quantified later in Section 2.4.

The entries in $[F]$ are rearranged here into a mass matrix $[M]$ and a stiffness matrix $[K]$:

$$[F]_{6 \times 6} = [K]_{6 \times 6} - \omega^2 [M]_{6 \times 6} \quad (32)$$

The mass matrix $[M]$ describes the masses of the pipes and the added masses attached to the pipes generated by the hydrodynamic pressures. The stiffness matrix $[K]$ is formed by the two pipes only since the fluids have no stiffness. The angular frequencies, ω , of the two fluid-filled pipes can be calculated using either Eq. (33), which was used by Chen and Rosenberg¹⁵, or Eq. (34), which is an alternative introduced here:

$$\det([F(\omega)]) = 0 \quad (33)$$

$$\text{eig}([M]^{-1}[K]) \rightarrow (\omega^2, \phi) \quad (34)$$

where $\det(\cdot)$ is the operator for calculating the determinant of a matrix, and $\text{eig}(\cdot)$ is the operator for calculating the eigenvalues and eigenvectors of a matrix. The determinant of $[F(\omega)]$ is a six-degree polynomial function of ω , and so Eq. (33) generates six roots (solutions) for ω . The dimensions of $[M]^{-1}[K]$ are 6×6 , and so Eq. (34) generates six eigenvalues and six eigenvectors. The square roots of the eigenvalues are the angular frequencies ω . The six values of ω calculated using Eqs. (33) and (34) are identical. Chen and Rosenberg¹⁵ calculated ω using Eq. (33), but the use of Eq. (34) is recommended here because it is computationally more efficient and provides six eigenvectors ϕ , which are the modal shapes of the two fluid-filled pipes. The modal shapes ϕ account for the interaction of the pipes and fluid. The modal shapes ϕ that are associated with the smallest two values of ω involve *coupled* lateral motions, termed “coupled modes” hereafter. The other four modal shapes are associated with axial and torsional motions of each pipe, which are not the focus of this paper and not discussed further. The shapes of the first and second coupled modes involve *out-of-phase* and *in-phase* motions of the two pipes, respectively. Their lateral displacements are associated with the assumed wavelength l . Figures 4a and b illustrate the two coupled modes for two concentric pipes supported at their tops with $l = 3.35 H$, namely the first wavelength for a cantilever (see Section 2.1). In the out-of-phase mode of Figure 4a (first coupled mode), the inner pipe displaces opposite to and more than the outer pipe. In the in-phase mode of Figure 4b (second coupled mode), the two pipes displace in the same direction with similar amplitudes. Additional information on the modal lateral displacements of the pipes is discussed in Section 2.2.

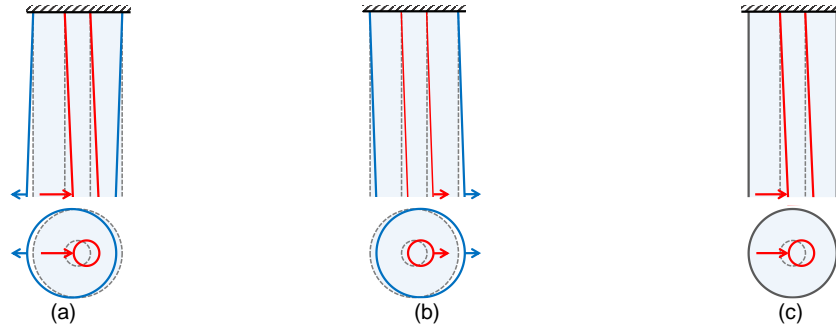


Figure 4. Modal shapes of lateral motions of two top-supported fluid-filled concentric pipes, $l = 3.35 H$: (a) out-of-phase mode; (b) in-phase mode; (c) uncoupled mode of the inner pipe

If the outer pipe is rigid, the degrees of freedom of the outer pipe (\bar{u}_{s2} , \bar{v}_{s2} , and \bar{w}_{s2}) in the equilibrium equations per Eq. (22) are set to zero. Accordingly, $[F_1]$, which is extracted from $[F]$ and associated with the \bar{u}_{s1} , \bar{v}_{s1} , and \bar{w}_{s1} -components, is used for the calculation of the frequencies of the inner pipe. The dimensions of $[F_1]$ are 3×3 , and so three values for ω are generated per Eqs. (33) or (34) with $[F]$ replaced by $[F_1]$. The smallest value of ω is associated with a lateral mode of the inner pipe, and the other two are associated with an axial and a torsional mode. The lateral frequency of the inner pipe is affected only by the hydrodynamic pressures due to its motion because the rigid outer pipe does not displace and induce pressures. Different from the coupled modal shapes of the two pipes presented in Figures 4a and b, the lateral frequency calculated using $[F_1]$ describes the “uncoupled mode” of the inner pipe, as the shape shown in Figure 4c for $l = 3.35 H$. Although $[F_1]$ does not consider the degrees of freedom of the rigid outer pipe, the calculation of the frequencies of the inner pipe involves the use of the radius of the outer pipe R_2 : see α_2 in a_{16} per Eq. (28). Figure 5 shows two pairs of fluid-filled concentric pipes, including identical flexible

inner pipes and rigid outer pipes with different radii. The frequencies of the two inner pipes are different and depend on the radii of the outer pipes, which define the dimensions of the fluid in the annulus. The frequency of the inner pipe of Figure 5b is lower than that of Figure 5a due to a greater added mass, although the volume of the annular fluid of Figure 5b is smaller (i.e., R_2/R_1 is smaller). Detailed information on the relationship between the frequency, added mass, and R_2/R_1 is presented in Section 2.2.



Figure 5. Two pairs of fluid-filled concentric pipes, including identical flexible inner pipes and rigid outer pipes with different radii: (a) larger outer pipe; (b) smaller outer pipe

2.2 Results

The corrected analytical solutions for two fluid-filled concentric pipes are used herein to calculate lateral frequencies for 1) the two coupled modes of the two pipes (out-of-phase and in-phase) and 2) the uncoupled mode of the inner pipe (considering the outer pipe to be rigid). The 6×6 matrix $[F]$ and the 3×3 submatrix $[F_1]$ per Eq. (22) are used in the eigen analysis per Eq. (34) for the coupled and uncoupled modes, respectively. The angular frequencies of lateral modes, which are square roots of eigenvalues, are denoted as ω_{lat} . The two pipes are assumed to be both cantilevers, and the first wavelength is used for the calculation: $l = 3.35 H$. Lateral frequencies associated with different boundary conditions and modal shapes can be calculated using the corresponding wavelengths l . (Analytical results for simply-supported pipes can be found in the report².)

The two pipes are assumed to be fabricated using an identical material. This assumption is reasonable for liquid-filled advanced reactors because the vessel (outer pipe) and the internal components (inner pipe) are generally fabricated using stainless and alloy steels^{1,22}, for which the mechanical properties are essentially identical. Consequently, the subscripts “1” and “2” for the mechanical properties of the inner and outer pipes, respectively, used in the analytical solutions are set aside hereafter: $E_1 = E_2 = E$, $\nu_1 = \nu_2 = \nu$, and $\rho_{s1} = \rho_{s2} = \rho_s$. The inner pipe is submerged in a fluid confined by the outer pipe, and so the densities of Fluids 1 and 2 are identical: $\rho_1 = \rho_2 = \rho$.

To generalize the analytical results for different dimensions and mechanical properties of pipes and fluids, the frequencies of the lateral modes f_{lat} are expressed as follows:

$$f_{lat} = \frac{\omega_{lat}}{2\pi} = C_{lat} \frac{1}{R_1} \sqrt{\frac{Eh_1}{\rho R_1}} \quad (35)$$

where the coefficient C_{lat} describes a *unitless frequency* normalized using the elastic modulus and dimensions of the inner pipe and the density of the fluid: E , R_1 , h_1 , and ρ . The coefficient C_{lat} is *insensitive* to (if $\rho_s \gg \rho$ and $\nu_s^2 \ll 1$) or independent of the mechanical properties of the pipes and the fluid (E , ν , ρ_s , and ρ), but dependent on the radii and height of the pipes (R_1 , R_2 , and H). Accordingly, the values of C_{lat} are presented here for a range of height-to-radius ratios and radius ratios: $5 \leq H/R_1 \leq 30$, and $R_2/R_1 = 1.2, 2, 5, \text{ and } 10$. These ratios are practical for the dimensions of liquid-filled nuclear reactors. Using Figure 1¹ as an example, the H/R_1 associated with the orange and blue lines are 23 and 7, respectively, and the R_2/R_1 associated with the red, green, and purple lines are 5, 1.5, and 9, respectively. Ratios of the wall thickness to the radius of reactor vessels and the internal components typically range between 0.0025 and 0.004 (ratios of diameter to wall thickness were estimated to be between 500 and 800²³). Accordingly, h_1/R_1 and h_2/R_2 used in the calculation of C_{lat} here are both assumed to be 0.003. However, for the dimensions and boundary condition considered here, C_{lat} is not sensitive to thickness-to-radius ratios ranging from 0.0005 to 0.008, if an identical value is used for both pipes: $h_1/R_1 = h_2/R_2$. (The difference in C_{lat} calculated using $h_1/R_1 = h_2/R_2 = 0.0005$ and 0.008 is less than 10%.) The two concentric pipes used here are assumed to be fabricated from stainless steel and the contained fluid is assumed to be liquid sodium, for which the mechanical properties used in the calculations are listed in the second column of Table 1. Again, C_{lat} , is insensitive to or independent of the mechanical properties of the pipes and fluid, and so the results presented here can be applied to pipes of a different material, and filled with a different fluid.

Table 1. Mechanical properties of the pipes and fluid used for the analytical solutions of Chen and Rosenberg and the numerical models

Pipes	Stainless steel	Carbon steel
Elastic modulus E (N/m ²)	1.9×10^{11}	2×10^{11}
Poisson's ratio ν	0.3	0.27
Density ρ_s (kg/m ³)	8000	7850
Fluid	Liquid sodium	Water
Density ρ (kg/m ³)	968	1000

Figure 6 presents C_{lat} for the cantilever pipes for $R_2/R_1 = 1.2, 2, 5,$ and 10 in four panels. For a given R_2/R_1 and H/R_1 , the value of C_{lat} for the out-of-phase mode (first coupled mode; red solid line) is appreciably smaller than that of the in-phase mode (second coupled mode; blue solid line), and C_{lat} for the uncoupled mode (black dotted line) lies between them. Namely, for two fluid-filled concentric pipes with given dimensions and mechanical properties, the lateral frequency of the in-phase mode is the highest, followed by the uncoupled mode of the inner pipe, and that of the out-of-phase mode is the lowest. The value of C_{lat} for the out-of-phase mode moves closer to that for the uncoupled mode with increasing R_2/R_1 and becomes identical at $R_2/R_1 = 5$ and 10 : see red solid and black dotted lines in Figures 6c and d. To investigate why the frequencies of the out-of-phase and uncoupled modes are identical with $R_2/R_1 \geq 5$, the lateral displacements of the pipes in these two modes are compared next.

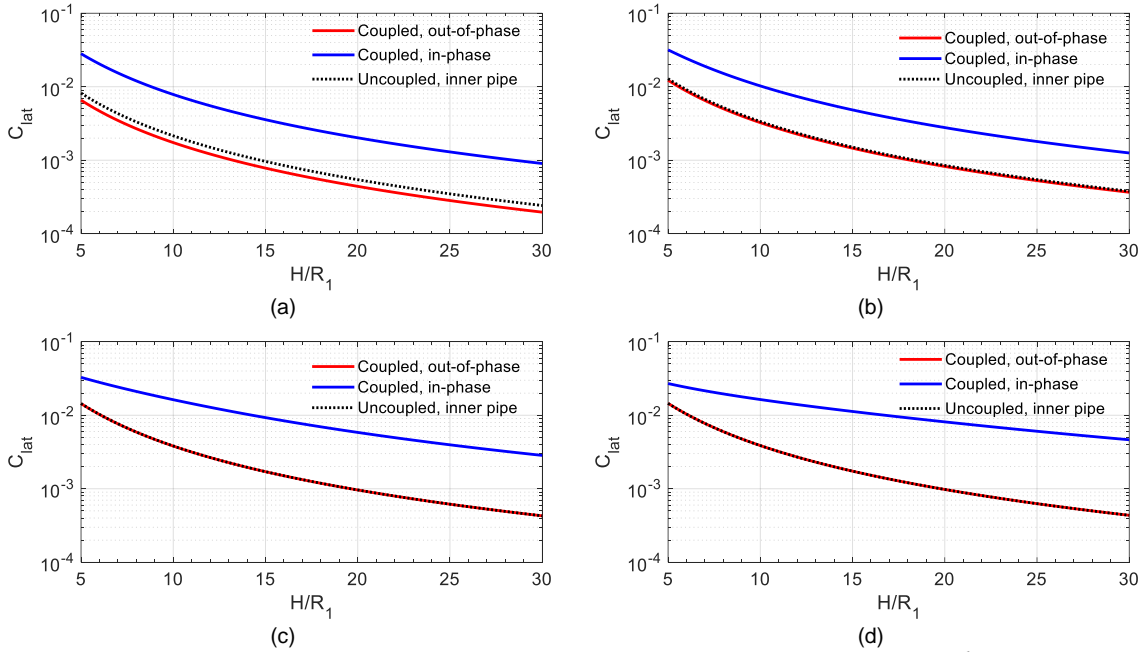


Figure 6. Frequency coefficients for two fluid-filled concentric pipes, cantilever, $l = 3.35 H, 5 \leq H/R_1 \leq 30$, coupled modes and uncoupled mode of the inner pipe: (a) $R_2/R_1 = 1.2$; (b) $R_2/R_1 = 2$; (c) $R_2/R_1 = 5$; (d) $R_2/R_1 = 10$

The amplitudes of the modal lateral displacements of the two pipes are the \bar{w}_{s1} - and \bar{w}_{s2} -components of the eigenvector ϕ per Eq. (34). Figure 7 presents the amplitudes of the two pipes in the out-of-phase mode (red solid and dashed lines) and in-phase mode (blue solid and dashed lines), and that of the inner pipe in the uncoupled mode (black dotted lines), for $H/R_1 = 20$ and $1.2 \leq R_2/R_1 \leq 10$. In the out-of-phase mode, the amplitude of the inner pipe (red solid line) is positive and that of the outer pipe (red dashed line) is negative; in the in-phase mode, the amplitudes of both pipes (blue solid and dashed lines) are positive, consistent with the lateral directions shown in Figures 4a and b. In the out-of-phase mode, the amplitude of the inner pipe increases and moves closer to that in the uncoupled mode with increasing R_2/R_1 , but the amplitude of the outer pipe reduces to zero for $R_2/R_1 \geq 4$. If the amplitude of the outer pipe is zero in the out-of-phase mode, it can be considered as *rigid* and *uncoupled* to the motion of the inner pipe.

Consequently, C_{lat} of the out-of-phase and uncoupled modes shown in Figures 6c and d are identical for $R_2/R_1 = 5$ and 10, respectively. Further, with increasing R_2/R_1 , the amplitudes of the inner and outer pipes in the in-phase mode increase and decrease, respectively, but they are not significantly different.

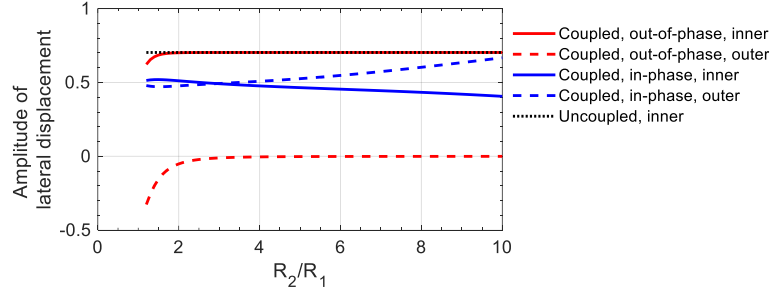


Figure 7. Amplitudes of modal lateral displacements of the two fluid-filled concentric pipes, cantilever, out-of-phase, in-phase, and uncoupled modes, $H/R_1 = 20$ and $1.2 \leq R_2/R_1 \leq 10$, $l = 3.35 H$

Per Figure 6, C_{lat} for all three modes reduce with increasing H/R_1 . This outcome is expected because the stiffness of a slenderer pipe (i.e., greater H/R_1) is smaller, and so the frequency is lower. Given a value of H/R_1 , C_{lat} of all three modes increase with increasing R_2/R_1 . Namely, for an inner pipe of given R_1 and H , the frequencies are higher if the radius of the outer pipe R_2 is greater. (Accordingly, the uncoupled frequency of the inner pipe of Figure 5a is higher than that of Figure 5b.) The added masses on the pipes generated by the hydrodynamic pressures are calculated to investigate the reason why the frequencies increase with increasing R_2/R_1 .

Accelerating in the $+x$ direction, the hydrodynamic pressures ($p_{1,1} - p_{1,2}$) on the inner pipe and $p_{2,2}$ on the outer pipe shown in Figure 3b generate resultant shear forces in the $-x$ direction (against the movement of the pipes). These hydrodynamic shear forces (excluding the inertial forces on the pipes) per unit length are the integrals of the pressures on the two pipes with respect to their perimeters, per the second terms of Eqs. (36) and (37):

$$S_{1,x} = \int_0^{2\pi} (p_{1,1} - p_{1,2})R_1 \cos \theta d\theta = M_{1,1} \cdot w_{s1}'' / \cos \theta + M_{1,2} \cdot w_{s2}'' / \cos \theta \quad (36)$$

$$S_{2,x} = \int_0^{2\pi} p_{2,2}R_2 \cos \theta d\theta = M_{2,1} \cdot w_{s1}'' / \cos \theta + M_{2,2} \cdot w_{s2}'' / \cos \theta \quad (37)$$

where $S_{1,x}$ and $S_{2,x}$ are hydrodynamic shear forces per unit length on the inner and outer pipes, respectively; and $p_{1,1}$, $p_{1,2}$, and $p_{2,2}$ are given by Eqs. (19), (20), and (21), respectively. The hydrodynamic shear forces are equivalent to the inertial forces of the fluid that is attached to and accelerates with the pipes in the x direction. This engaged fluid is the added mass on the pipes, which reduces their lateral frequencies. Per the third terms of Eqs. (36) and (37), $S_{1,x}$ and $S_{2,x}$ are related to the added masses (per unit length), $M_{1,1}$, $M_{1,2}$, $M_{2,1}$, and $M_{2,2}$, and the accelerations of the pipes in the x direction, $w_{s1}'' / \cos \theta$ and $w_{s2}'' / \cos \theta$. Both $M_{1,1}$ and $M_{1,2}$ contribute to $S_{1,x}$ on the inner pipe and are associated with the motion of the inner pipe and its interaction with the outer pipe, respectively. Similarly, $S_{2,x}$ on the outer pipe is a function of $M_{2,1}$ and $M_{2,2}$, which are associated with its interaction with the inner pipe and the motion of the outer pipe, respectively.

Added masses are calculated per Eqs. (36) and (37) for the upper internal of Figure 1. The radius of the upper internal is 1 m, and the radius and height of the vessel (tank) are 5 m and 20 m, respectively: all approximated from Figure 1. The upper internal is assumed here to be a submerged (inner) pipe enclosed by a cylindrical tank wall (outer pipe) with a range of radii: $R_1 = 1$ m, $H = 20$ m, and $1.2 \text{ m} \leq R_2 \leq 5$ m. The mechanical properties of stainless steel and liquid sodium listed in Table 1 and $h_1/R_1 = h_2/R_2 = 0.003$ are used for the calculation. Both pipes are assumed to be head-supported, and the first wavelength for cantilevers is used for the calculation: $l = 3.35 H$. Figure 8a presents the calculated added masses (per unit length): $M_{1,1}$ and $M_{2,2}$ (blue solid and red dashed lines) are positive, and $M_{1,2}$ and $M_{2,1}$ (blue dashed and red solid lines) are negative. Accordingly, if one of the two concentric pipes moves in the $+x$ direction (i.e., positive $w_{s1}'' / \cos \theta$ or $w_{s2}'' / \cos \theta$), the added mass on this pipe (i.e., $M_{1,1}$ or $M_{2,2}$) generates a positive inertial force, and that on the other pipe (i.e., $M_{1,2}$ or $M_{2,1}$) generates a negative inertial force. As seen in Figure 8a, the total added mass (black dash-dotted line) increases with increasing R_2/R_1 due to the greater volume of the fluid in the annulus between the pipes. This total added mass is almost identical to but less than the total fluid mass

(per unit length; $\rho\pi R_2^2$; light blue line): a significant fraction of the fluid is involved in the lateral motion of the pipes associated with the assumed wavelength $l = 3.35 H$. The absolute values of $M_{1,1}$, $M_{1,2}$, and $M_{2,1}$ all reduce with increasing R_2/R_1 , whereas $M_{2,2}$ increases significantly and is the greatest of the four.

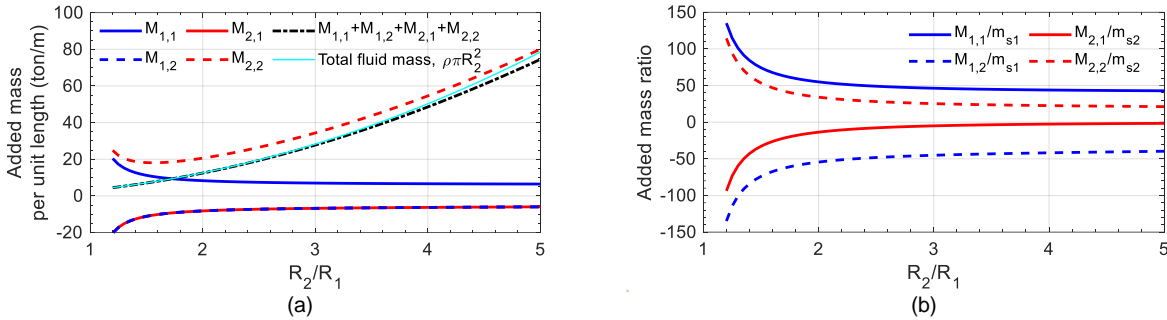


Figure 8. Added masses on fluid-filled concentric pipes, $R_1 = 1$ m, $H = 20$ m, $1.2 \leq R_2/R_1 \leq 5$, $h_1/R_1 = h_2/R_2 = 0.003$, $l = 3.35 H$: (a) added mass per unit length; (b) ratios of the added mass to the mass of the pipe, $m_{s1} = 2\pi R_1 h_1 \rho_s$ and $m_{s2} = 2\pi R_2 h_2 \rho_s$

Figure 8b presents the ratios of the added mass to the mass of the corresponding pipe (termed hereafter the added-mass ratio), calculated using the data presented in Figure 8a. The masses of the inner and outer pipes (per unit length) are $m_{s1} = 2\pi R_1 h_1 \rho_s$ and $m_{s2} = 2\pi R_2 h_2 \rho_s$, respectively. Per Figure 8b, the absolute values of the four added-mass ratios all reduce with increasing R_2/R_1 . Accordingly, given a value of H/R_1 , the frequencies, for which the coefficients C_{lat} are presented in Figure 6, increase with increasing R_2/R_1 due to the reduced added-mass ratios.

Fritz¹⁶ derived analytical solutions of added masses for a rigid solid cylinder submerged in a fluid confined by a concentric rigid pipe. The digital appendix to this paper identifies differences in calculated added mass for the solutions derived herein and those of Fritz.

2.3 Calculations of Frequencies for Submerged Components

The lateral frequencies for three pairs of fluid-filled, concentric, cylindrical pipes are calculated for 1) the two coupled modes, and 2) the uncoupled mode of the inner pipe (assuming the outer pipe to be rigid). One of the three pairs is based on nuclear components: the reactor vessel and reactor jacket in the prototype fast reactor (PFR) presented in Figure 9a. The other two pairs are those used for the numerical models in Section 3, as shown in Figure 10: M1 and M2.

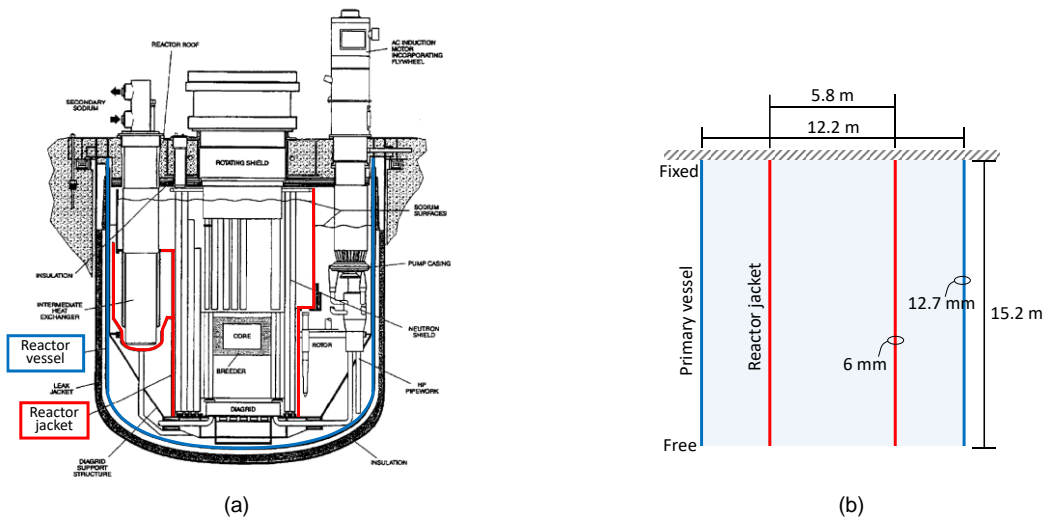


Figure 9. Nuclear components: (a) PFR, Dounreay, Scotland²⁴; (b) N1, simplifying the geometries and boundary conditions of the reactor vessel and reactor jacket for the analytical solutions

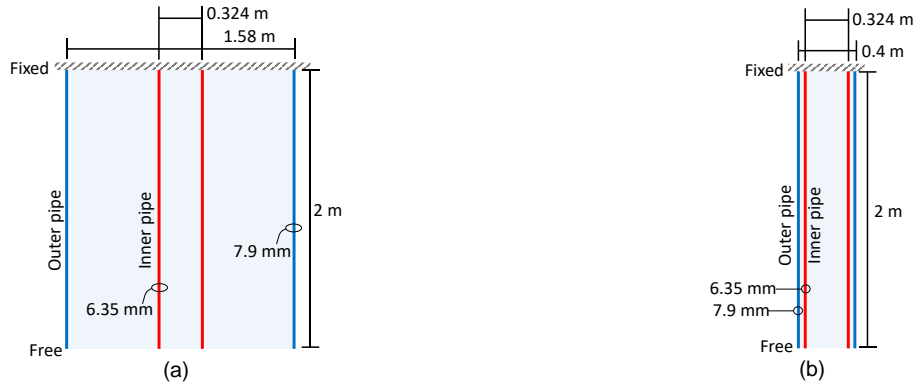


Figure 10. Dimensions and boundary conditions for two pairs of fluid-filled concentric pipes: (a) M1, based on specimens of the earthquake-simulator tests; (b) M2, enabling calculations of coupling between the two pipes

The reactor vessel and reactor jacket in the PFR are identified in blue and red, respectively, in Figure 9a. The reactor vessel was constructed using stainless steel and filled with liquid sodium²⁵. The reactor jacket in the vessel was a stainless steel shell²⁵. To employ the analytical solutions, their geometries are simplified to two fluid-filled, concentric, cylindrical pipes shown in Figure 9b, denoted as N1. Other components internal to the vessel are ignored, and the free surface of the liquid sodium is not considered to accommodate the assumption of the analytical solutions. The radius, height, and wall thickness of the reactor vessel are applied to the outer pipes in N1: $R_2 = 6.1$ m, $H = 15.2$ m, and $h_2 = 12.7$ mm²⁵. The radius of the inner pipe, R_1 , is assumed to be 2.9 m, estimated based on the bottom end of the reactor jacket shown in Figure 9a. Somewhat arbitrarily, the wall thickness of the inner pipe, h_1 , is assumed to be 6 mm, to achieve a wall thickness-to-radius ratio identical to that of the outer pipe: $h_1 / R_1 = h_2 / R_2 = 0.0021$. (The dimensions of the reactor jacket are not available in prior studies and documents, to the knowledge of the authors.) To be consistent with the assumptions used in the analytical solutions, the height and boundary conditions of the inner pipe must be identical to those of the outer pipe. Given that the reactor vessel is supported at its head, the two pipes in N1 are assumed to be top-supported. The dimensions used for N1 are listed in the second row of Table 2. The mechanical properties of stainless steel and liquid sodium listed in Table 1 are used for the calculation.

Table 2. Dimensions used for the analytical solutions for two fluid-filled concentric pipes shown in Figures 9b and 10

	R_1 (m)	R_2 (m)	h_1 (mm)	h_2 (mm)	H (m)	R_2 / R_1	H / R_1	$h_1 / R_1, h_2 / R_2$
N1	2.9	6.1	6	12.7	15.2	2.1	5.2	0.0021
M1	0.162	0.79	6.35	7.92	2	5.2	12.3	0.04
M2	0.162	0.2	6.35	7.92	2	1.2	12.3	0.04

The dimensions of M1 noted in Figure 10a are based on specimens used for earthquake-simulator tests⁸⁻¹⁰ that will support validation of the numerical models presented in Section 3. (The models are verified in this paper and will then be validated elsewhere.) The height, radius, and wall thickness of the outer pipe in M1 are identical to those of the test tank used for the experiments: $H = 2$ m, $R_2 = 0.79$ m, and $h_2 = 7.92$ mm. The radius and wall thickness of the inner pipe in M1 are identical to those of the central component in the test tank: a round HSS 12.75 × 0.25 steel pipe with $R_1 = 0.162$ m and $h_1 = 6.35$ mm. The ratio of the radii of the two concentric pipes (or the test tank to the central component) is around 5, which is reasonable for prototype advanced reactors. Per the red lines in Figure 1, the ratio of the radii of the vessel to the upper internal is 5. Per Sections 2.1 and 2.2, two concentric pipes are coupled, as shown in Figures 4a and b, if the annulus between pipes is relatively narrow (e.g., $R_2 / R_1 \leq 4$). The dimensions of M2 enable calculations of the coupled response. The inner pipe is identical to that used for M1. The height and the wall thickness of the outer pipe are identical to those used for M1, but the radius is reduced: $R_2 = 0.2$ m. The pipes of M1 and M2 are all top-supported. The dimensions for M1 and M2 are listed in the third and fourth rows of Table 2, respectively. To be consistent with the test specimens, the mechanical properties of carbon steel and water listed in Table 1 are used for the calculations.

Below, the lateral frequencies associated with the first wavelength $l = 3.35 H$ of cantilevers are calculated for N1, M1, and M2. The frequency coefficient C_{lat} , which is suitable for reactor components with typical wall thickness-to-radius ratios ($h_1/R_1 = h_2/R_2 \approx 0.003$ per Section 2.2), is used for N1: per values in Figure 6b for $R_2/R_1 = 2$ and extracted at $H/R_1 = 5.2$. Table 3 lists C_{lat} for 1) the out-of-phase mode, 2) the in-phase mode, and 3) the uncoupled mode of the inner pipe, and the corresponding frequencies f_{lat} calculated per Eq. (35) for N1.

The frequency coefficients C_{lat} presented in Figure 6 do not apply to M1 and M2 because their geometric ratios $h_1/R_1 = h_2/R_2 = 0.04$ are an order of magnitude greater than those of nuclear components and beyond the range accommodated by C_{lat} ($h_1/R_1 = h_2/R_2 = 0.0005$ to 0.008). The frequencies of M1 and M2 are calculated using the analytical process presented in Section 2.1. Matrices $[F]$ and $[F_i]$ per Eq. (22) are constructed for each of M1 and M2 using the entries per Eqs. (23) to (31). Matrices $[F]$ and $[F_i]$ are used in the eigen analysis per Eq. (34) for the coupled and uncoupled modes, respectively. The lateral frequencies f_{lat} calculated using the eigenvalues are listed in Table 3.

Table 3. Lateral frequencies of the two fluid-filled concentric pipes shown in Figures 9b and 10, first wavelength $l = 3.35 H$

Mode	Coupled, out-of-phase		Coupled, in-phase		Uncoupled, inner pipe	
	C_{lat}^1	f_{lat} (Hz)	C_{lat}^1	f_{lat} (Hz)	C_{lat}^1	f_{lat} (Hz)
N1	0.0113	2.5	0.0293	6.6	0.0119	2.6
Frequency	f_{lat} (Hz)		f_{lat} (Hz)		f_{lat} (Hz)	
M1	37.9		98.9		38.0	
M2	20.9		63.7		24.7	

1. Extracted from Figure 6b at $H/R_1 = 5.2$

2.4 Identification and Quantification of Errors in Chen and Rosenberg

Errors were made in the derivation of Chen and Rosenberg¹⁵ for a_{16} , a_{26} , a_{17} , and a_{27} in $[F]$, all of which relate the inertial and hydrodynamic forces on the pipes to their radial displacements per Section 2.1. Table 4 lists the original a_{16} , a_{26} , a_{17} , and a_{27} derived by Chen and Rosenberg¹⁵ and the equation numbers of their counterparts corrected in this paper: Eqs. (28), (29), (30), and (31). The listed original entries are expressed using unitless parameters defined by Chen and Rosenberg¹⁵: $\delta_1 = h_1/R_1$, $\delta_2 = h_2/R_2$, $\mu_1 = \rho_1 R_1 / (\rho_{s1} h_1)$, $\mu_2 = \rho_2 R_2 / (\rho_{s2} h_2)$, $\Omega_1 = R_1 \omega \sqrt{\rho_{s1} (1 - \nu_1^2) / E_1}$, and $\Omega_2 = R_2 \omega \sqrt{\rho_{s2} (1 - \nu_2^2) / E_2}$. The parts of the entries involving mistakes are bolded in Table 4, which are all factors for terms including the modified Bessel functions, I_1 , K_1 , I_1' , and K_1' . These Bessel functions are used for calculating hydrodynamic pressures on the pipes shown in Figure 3b. One of the errors was made to a sign used for a_{16} : see the bolded sign in the second row of Table 4 and Eq. (28). Entry a_{16} should relate $p_{1,1} - p_{1,2}$ on the inner pipe shown in Figure 3b to its radial displacement $w_{s,1}$, but Chen and Rosenberg¹⁵ incorrectly used $p_{1,1} + p_{1,2}$ in the derivation. The incorrect direction (sign) defined for $p_{1,2}$ made the pipes unstable and results in imaginary values for their frequencies. Other errors were made in the use of the chain rule for the derivatives of the Bessel functions with respect to r (i.e., I_1' and K_1'). Comparing the bolded factors shown in Table 4 and their counterparts per Eqs. (28) to (31), factors of $1/R_1$ or $1/R_2$ were omitted incorrectly in the original entries.

Table 4. Entries a_{16} , a_{26} , a_{17} , and a_{27} in $[F]$, presented by Chen and Rosenberg¹⁵ (errors bolded) and corrected in this paper

Entries	Original equations involving errors, per Eq. (15) ¹⁵	Corrected equations
a_{16}	$1 + \frac{\delta_1^2}{12} (\alpha_1^4 + 2\alpha_1^2) - \Omega_1^2 \cdot (1 + \mu_1 \frac{I_1(\alpha_1)}{I_1'(\alpha_1)} + \mu_1 \frac{\rho_2}{\rho_1} \frac{I_1(\alpha_1)K_1'(\alpha_2) - K_1(\alpha_1)I_1'(\alpha_2)}{I_1'(\alpha_1)K_1'(\alpha_2) - K_1'(\alpha_1)I_1'(\alpha_2)})$	Eq. (28)
a_{26}	$1 + \frac{\delta_2^2}{12} (\alpha_2^4 + 2\alpha_2^2) - \Omega_2^2 \cdot (1 + \mu_2 \frac{K_1(\alpha_2)I_1'(\alpha_1) - I_1(\alpha_2)K_1'(\alpha_1)}{I_1'(\alpha_1)K_1'(\alpha_2) - K_1'(\alpha_1)I_1'(\alpha_2)})$	Eq. (29)
a_{17}	$\Omega_1^2 \cdot \mu_1 \frac{\rho_2}{\rho_1} \frac{R_2}{R_1} \frac{K_1(\alpha_1)I_1'(\alpha_1) - I_1(\alpha_1)K_1'(\alpha_1)}{I_1'(\alpha_1)K_1'(\alpha_2) - K_1'(\alpha_1)I_1'(\alpha_2)}$	Eq. (30)
a_{27}	$-\Omega_2^2 \cdot \mu_2 \frac{R_1}{R_2} \frac{I_1(\alpha_2)K_1'(\alpha_2) - K_1(\alpha_2)I_1'(\alpha_2)}{I_1'(\alpha_1)K_1'(\alpha_2) - K_1'(\alpha_1)I_1'(\alpha_2)}$	Eq. (31)

The original entries a_{16} , a_{26} , a_{17} , and a_{27} listed in Table 4 are used to construct $[F]$ and $[F_1]$ per Eq. (22) and generate C_{lat} per Eqs. (34) and (35). Data for C_{lat} generated using the original solutions are added and compared to those presented in Figure 6, as shown in Figure 11. The thin orange, light blue, and gray lines in each panel (if available) describe C_{lat} for a given R_2/R_1 , generated using the original solutions for out-of-phase, in-phase, and uncoupled modes, respectively. The red, blue, and black thick lines describe their corrected counterparts, which are identical to those shown in Figure 6. The results of the original solutions are complex values due to the mistake in the sign used for a_{16} , and only the real part is presented in Figure 11. If C_{lat} is an imaginary value (i.e., the real part is zero), no result is presented (e.g., the light blue line is not available in Figures 11a and b, Figure 11c for $H/R_1 \geq 7$, and Figure 11d for $H/R_1 \geq 21$).

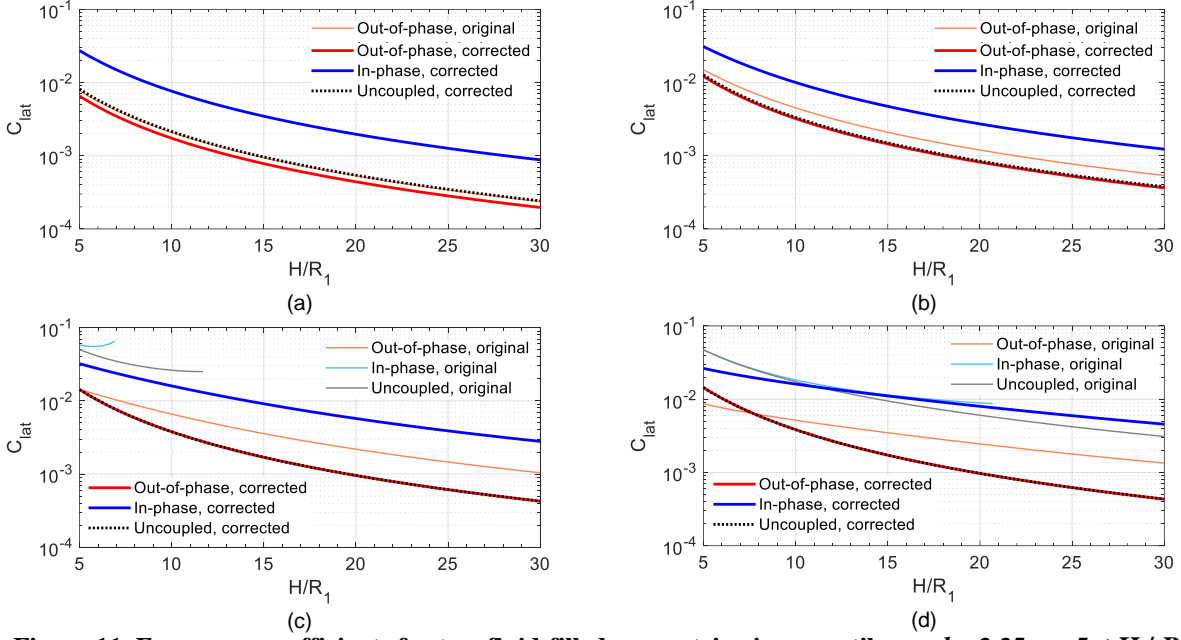


Figure 11. Frequency coefficients for two fluid-filled concentric pipes, cantilever, $l = 3.35 H$, $5 \leq H/R_1 \leq 30$, coupled modes and uncoupled mode of the inner pipe, calculated using the original and corrected a_{16} , a_{26} , a_{17} , and a_{27} for $[F]$ and $[F_1]$ listed in Table 4: (a) $R_2/R_1 = 1.2$; (b) $R_2/R_1 = 2$; (c) $R_2/R_1 = 5$; (d) $R_2/R_1 = 10$

The lateral frequencies are calculated using C_{lat} generated from the original solutions for N1 presented in Figure 9b: head-supported stainless-steel pipes filled with liquid sodium. The mechanical properties and dimensions ($R_2/R_1 = 2.1$ and $H/R_1 = 5.2$) are listed in Tables 1 and 2, respectively. Extracted from Figure 11b for $R_2/R_1 = 2$, C_{lat} at $H/R_1 = 5.2$ is 0.014 for the out-of-phase coupled mode (orange thin line), and the corresponding frequencies f_{lat} calculated per Eq. (35) is 3.1 Hz. Using the original solutions, f_{lat} is overestimated by 25%, by comparison with 2.5 Hz per Table 3 calculated using the corrected solutions (red thick line in Figures 11b or 6b). Due to the imaginary results calculated using the original solutions, C_{lat} are not available for the in-phase and uncoupled modes for N1, and the frequencies cannot be calculated.

3. NUMERICAL ANALYSIS AND VERIFICATION

The lateral frequencies of the submerged component of M1 and M2 shown in Figure 10, namely, the inner pipe, are calculated using numerical models and compared with analytical results listed in Table 3. The Arbitrary Lagrangian-Eulerian (ALE) and Incompressible Computational Fluid Dynamics (ICFD) solvers in LS-DYNA¹⁸ are used for numerical FSI analysis.

The frequencies of the submerged inner pipe are dependent on 1) its mass and stiffness and 2) the added mass generated by hydrodynamic pressures. If the fluid is not included, the frequencies of the inner pipe are dependent on its mass and stiffness only. To benchmark the numerical model of the inner pipe (involving no fluid) prior to the FSI analysis, numerical and analytical results of its first lateral frequency are compared. The fluid density used for the analytical

solutions is set to zero, namely, no fluid: $\rho_1 = \rho_2 = 0$ in Eqs. (28) to (31). The numerical models of the inner pipe are identical to those used for the FSI analysis, but the fluid is excluded. (The numerical models of the inner pipe shown as green in Figures 12a, d and 13a, d will be described later in Section 3.1.) The numerical and analytical results are identical: 78.4 Hz. Accordingly, for the submerged inner pipe, if the frequencies calculated using the ALE and ICFD models and analytical solutions are in good agreement, the added mass contributed by the hydrodynamic pressures on its surface is correctly calculated. The models that calculate the hydrodynamic pressures correctly are considered verified here for small-amplitude, unidirectional, horizontal inputs because other seismic FSI responses are all induced by these pressures. The hydrodynamic shear force and moment at the support of the inner pipe subjected to unidirectional horizontal inputs are associated with the resultant force of the hydrodynamic pressure on its surface. Wave heights are not considered in the verification since no free surface is included in the numerical and analytical calculations.

3.1 Numerical Models

Figure 12 presents the ALE models and the global coordinate system (x, y, z) for the numerical models of M1 and M2 per Figure 10. Figures 12a and d present the elements for the pipes of M1 and M2, respectively. The outer pipe is shown in dark blue and the inner pipe is shown in green. Figures 12b and e present the elements for the fluid of M1 and M2, respectively. The pipes are modeled using Lagrangian, four-node, shell elements, and the fluid is modeled using Eulerian, eight-node, solid elements. The pipes and the fluid share nodes at their interfaces. Figures 12c and f present the fluid filling the pipes for M1 and M2, respectively, at the first step of the analysis (time $t = 0$).

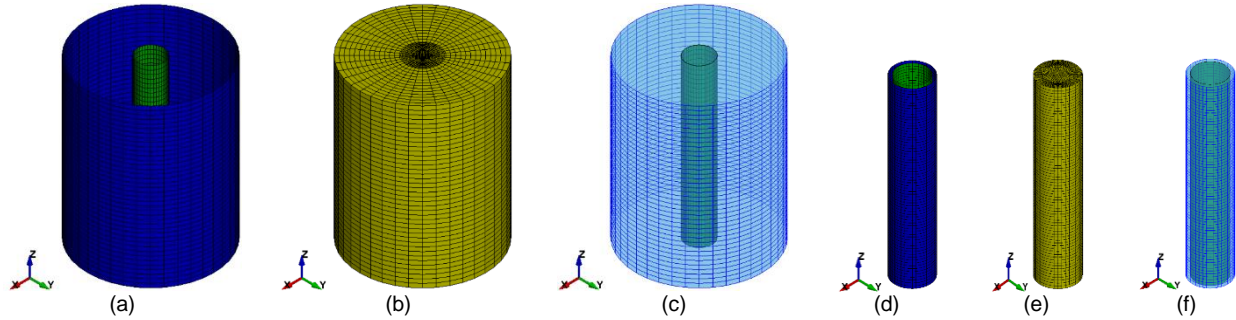


Figure 12. ALE models for two fluid-filled concentric pipes: (a) pipes of M1; (b) fluid of M1; (c) pipes and fluid of M1 at $t = 0$; (d) pipes of M2; (e) fluid of M2; (f) pipes and fluid of M2 at $t = 0$

Figure 13 presents the ICFD models and the global coordinate system (x, y, z) . Figures 13a and d show the elements for the pipes of M1 and M2, respectively: outer pipes in dark blue and the inner pipes in green. The model of the fluid is defined by its boundary surfaces. Figures 13b and e present half models to show the fluid surfaces for M1 and M2, respectively. The fluid domain in each model is defined using four surfaces: 1) adjacent to the outer pipe (yellow), 2) adjacent to the inner pipe (light blue), 3) horizontally at the top of the two pipes (pink), and 4) horizontally at the base of the two pipes (dark blue). The pipes are constructed using Lagrangian, four-node, shell elements, and the fluid surfaces are constructed using Lagrangian, three-node, shell elements. The pipes and the fluid surfaces do not share nodes at their interfaces. To model the interaction between the pipes and fluid, the *ICFD_BOUNDARY_FSI card is assigned to the fluid surfaces adjacent to the pipes: yellow and light blue in Figures 13b and e. The *MESH_EMBEDSHELL card is assigned to the light blue surface to model the fluid domain separated by the submerged shell elements of the inner pipe. The fluid domain is automatically meshed using Lagrangian, four-node, solid elements by the ICFD solver at $t = 0$: Figures 13c and f for M1 and M2, respectively.

Lateral frequencies are calculated using each model for 1) the coupled modes of the two pipes (out-of-phase and in-phase), and 2) the uncoupled mode of the inner pipe. To calculate the two coupled frequencies, the elements of both pipes in each model are assigned to be elastic. To calculate the uncoupled frequency, the elements of the inner pipe are assigned to be elastic, and those of the outer pipe are assigned to be rigid. Mechanical properties consistent with carbon steel per Table 1 are used for both elastic and rigid pipes. No damping is applied to the pipes. To enable a comparison between the numerical and analytical results, an ideal fluid is used in the numerical models: inviscid and incompressible. The fluid in the models is assigned the density of water, namely $\rho_w = 1000 \text{ kg/m}^3$, and a viscosity μ_w of 0 to be inviscid. Although the bulk modulus K_w of an incompressible fluid is infinite, the value of water $K_w = 2.15 \times 10^9 \text{ N/m}^2$ is used for the ALE models through the *EOS_LINEAR_POLYNOMIAL card (termed C1 in the card)

since water is sufficiently incompressible and a greater bulk modulus increases analysis time significantly. The bulk modulus is not used in the ICFD analysis because the solver can only accommodate incompressible fluids. The mass of each component of the numerical models is listed in Table 5. No gravitational acceleration is assigned to the models since hydrostatic pressure is not considered in the analytical solutions.

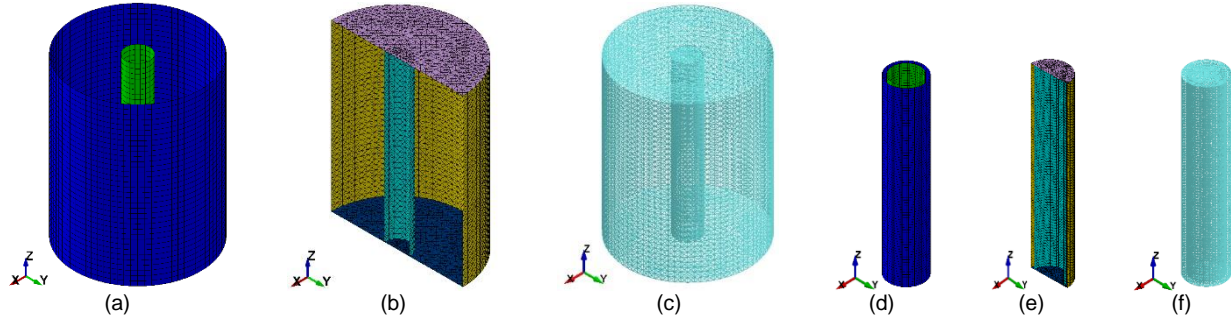


Figure 13. ICFD models for two fluid-filled concentric pipes: (a) pipes of M1; (b) fluid surfaces for M1; (c) fluid of M1 at $t = 0$; (d) pipes of M2; (e) fluid surfaces for M2; (f) fluid of M2 at $t = 0$

Table 5. Mass of each component in the ALE and ICFD models, pipes and water, M1 and M2

Components	Mass (kg)	
	M1	M2
Outer pipe	629	159
Inner pipe	103	103
Water	3921	251

The ALE and ICFD solvers cannot perform eigen analysis, and so frequencies are identified from the response histories of the submerged component (inner pipe) undergoing free vibration. The displacement time series shown in Figure 14a is applied at the free (bottom) end of the inner pipe in the x direction, and the pipe is then released to vibrate laterally. The peak displacement is 15 mm, which is less than 1% of the height of the inner pipe ($0.01 H = 20$ mm). This displacement generates the first lateral modal shape of the inner pipe, and the associated frequencies (i.e., two coupled and one uncoupled) are the focus of the analysis and verification. The circumferential, axial, and torsional modes are not considered. A rigid diaphragm is assigned to the nodes at the free end of the inner pipe in each model through *CONSTRAINT_NODAL_RIGID_BODY card, and the displacement time series is applied at the center of the diaphragm. The rigid diaphragm makes the assigned set of nodes translate and rotate as a rigid body, and prevents circumferential deformation due to the applied displacement. Figure 14b shows the rigid diaphragm using yellow lines in the ICFD model for M1. Response-history analysis for the ALE and ICFD models is performed for 2 seconds after the inner pipe is released (i.e., at 0.03 second per Figure 14a). The displacement time series of the free vibration at the center of the rigid diaphragm is transformed into the frequency domain using the Fast Fourier Transform (FFT). The frequencies of the inner pipe are identified from the Fourier amplitude spectra.

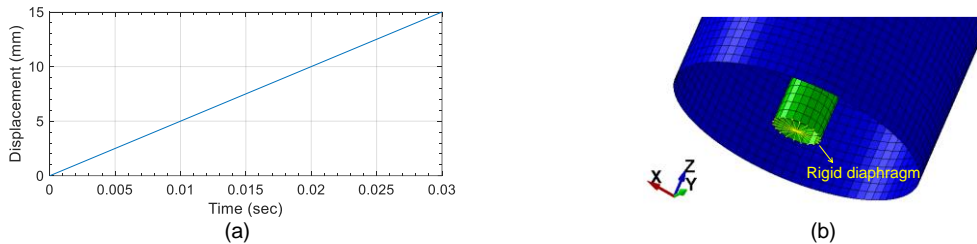


Figure 14. Displacement applied to the center of the rigid diaphragm at the free end of the inner pipe in the x direction: (a) displacement time series; (b) rigid diaphragm in the ICFD model for M1

3.2. Numerical Results and Verification

Figures 15a and b present Fourier amplitude spectra for the displacements at the center of the rigid diaphragm of the inner pipe of M1 and M2, respectively, calculated using the ALE models. Figures 15c and d present the companion

results for the ICFD models. Each Fourier amplitude spectrum is normalized by its maximum ordinate. The blue solid and red dashed lines are spectra for the displacement of the inner pipe, as the outer pipe is assigned to be elastic and rigid, respectively. The coupled frequencies are identified from the blue spectra, and the uncoupled frequencies are identified from the red spectra. Table 6 lists the frequencies identified from the peak(s) of each spectrum.

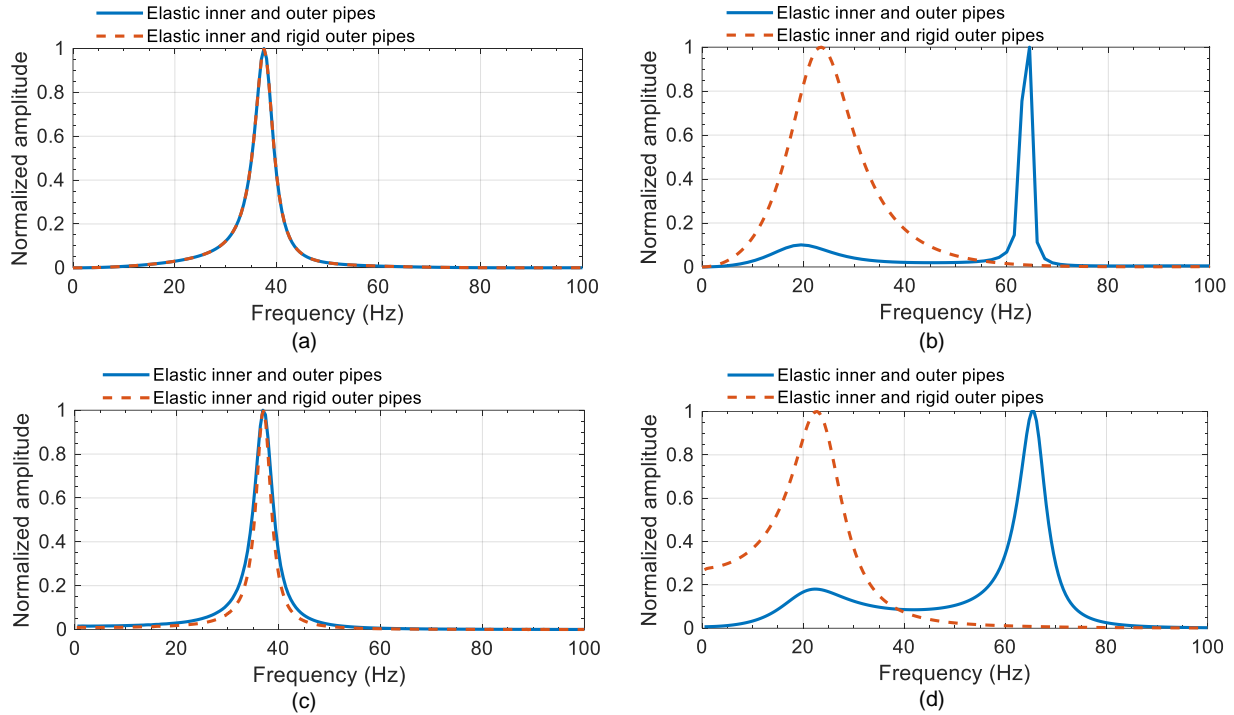


Figure 15. Normalized Fourier amplitude spectra for the displacement at the center of the rigid diaphragm of the inner pipe: (a) ALE model for M1, $R_2 / R_1 = 5.2$; (b) ALE model for M2, $R_2 / R_1 = 1.2$; (c) ICFD model for M1, $R_2 / R_1 = 5.2$; (d) ICFD model for M2, $R_2 / R_1 = 1.2$

Table 6. Coupled and uncoupled lateral frequencies of the inner pipe identified from the spectra of Figure 15, calculated using the ALE and ICFD models and the analytical solutions, M1 and M2

Model	Mode	Frequency (Hz)			Difference ¹ (%)	
		ALE model	ICFD model	Analytical solutions	ALE model	ICFD model
M1	First coupled, out-of-phase	38	37	38	-1	-2
	Second coupled, in-phase	-- ²	-- ²	99	--	--
	Uncoupled	38	37	38	-1	-2
M2	First coupled, out-of-phase	20	22	21	-3	4
	Second coupled, in-phase	64	65	64	1	2
	Uncoupled	24	24	25	-4	-5

1. Percentage differences of the numerical results with respect to those calculated using the analytical solutions

2. Not available since the modal displacement of the inner pipe is too small

For M1 with $R_2 / R_1 = 5.2$, per Figures 15a and c and Table 6, the frequencies of the first coupled and uncoupled modes are identical: 38 Hz for the ALE models and 37 Hz for the ICFD models. As noted in Section 2.2 (see discussion on pages 9 and 10), if the radii of two flexible fluid-filled pipes are sufficiently different (e.g., $R_2 / R_1 \geq 4$), the frequencies of the first coupled mode (out-of-phase mode) and uncoupled mode are identical. The blue spectra in Figures 15a and c do not show a peak associated with the second coupled mode (in-phase mode) because the modal displacement of the inner pipe is too small. For M2 with $R_2 / R_1 = 1.2$, per Figures 15b and d, two peaks at different frequencies are shown in each blue spectrum, which are associated with the two coupled modes. Per the blue spectra, the two coupled frequencies calculated using the ALE model are 20 and 64 Hz, and those calculated using the ICFD model are 22 and 65 Hz, all listed in Table 6. The uncoupled frequency is 24 Hz, identified from the red spectra

presented in Figures 15b and d for both models. The uncoupled frequency lies between the two coupled frequencies, which is consistent with the analytical results shown in Figure 6 for $R_2 / R_1 \leq 2$.

The widths of the peaks in the presented spectra are associated with damping effects on the fluid-filled pipes. Since the fluid is inviscid and no damping is assigned to the elements of the pipes in the numerical models, the damping effect is only associated with the fluid pressure that is opposite to and reduces the movement of the free-vibrating inner pipe: the so-called *pressure drag*. The half-power bandwidth method²⁶ is used for the spectra to calculate the damping ratio of each mode for the inner pipe. Per the spectra in Figures 15a and c, the damping ratios of the uncoupled and out-of-phase modes of M1 ($R_2 / R_1 = 5.2$) are both around 3%. Calculating using Figures 15b and d for M2 ($R_2 / R_1 = 1.2$), the damping ratios of the out-of-phase, in-phase, and uncoupled modes are around 25%, 3%, and 20%, respectively. Accordingly, the damping effect is generally greater with smaller R_2 / R_1 : an internal component (inner pipe) submerged in a fluid confined by a relatively small tank (outer pipe).

The frequencies of the inner pipes in M1 and M2 calculated using the models and analytical solutions are compared to verify the ALE and ICFD models. The fifth column of Table 6 lists the analytically calculated frequencies, which are extracted from Table 3. The differences between the numerical and analytical results are small ($\leq 5\%$), listed in the sixth and seventh columns of Table 6 for the ALE and ICFD models, respectively.

4. SUMMARY, CONCLUSIONS, AND RECOMMENDATIONS

Earthquake shaking of a liquid-filled advanced reactor induces fluid-structure interaction (FSI) between the reactor vessel, the submerged internal components, and the contained liquid. Verified and validated numerical models for FSI analysis will be required for seismic design, qualification, and risk assessment of advanced reactors. This paper verifies numerical models for internal components subjected to small-amplitude, unidirectional, horizontal motion using analytical solutions of Chen and Rosenberg¹⁵ as corrected herein. The analytical solutions are re-derived in this paper, and the errors made by Chen and Rosenberg¹⁵ are identified and corrected. The solutions are derived for lateral frequencies of two concentric cylindrical pipes filled with liquid (fluid). The inner pipe is an internal component, and the outer pipe refers to the wall of a reactor vessel or tank. The calculated frequencies accommodate effects of unidirectional lateral shaking (i.e., horizontal shaking if the pipes are vertical): 1) the interaction of the two pipes with the presence of the fluid, and 2) hydrodynamic pressures on the surfaces of the pipes. The lengths and boundary conditions of the two pipes are identical. The pipes are either rigid or elastic, and the fluid is ideal. A unitless coefficient for the lateral frequencies is defined. The coefficient is presented for pipes with a range of dimensions for application to advanced reactors, and can be used for different fabricating materials and filling fluids. The presented data are suitable for the preliminary seismic design of submerged cylindrical components. The presented data are suitable for the preliminary seismic design of submerged cylindrical components.

To be consistent with the analytical solutions and to enable verification, numerical models are developed for two pairs of fluid-filled concentric pipes: M1 and M2. Seismic FSI analysis is performed using the ALE and ICFD solvers in LS-DYNA. The frequencies of the inner pipe of M1 and M2 calculated using the numerical models and the (corrected) analytical solutions are compared, and the differences are very small ($\leq 5\%$). The frequencies can be correctly predicted only if the models calculate the hydrodynamic pressure on the surfaces of the pipes accurately. Other responses (e.g., reactions at the support) to unidirectional lateral (horizontal) inputs are all generated by the hydrodynamic pressure. Consequently, the ALE and ICFD models, which calculate the lateral frequencies correctly, are considered to be verified here for unidirectional lateral (horizontal) motions of a small amplitude. Although the verification procedures were developed for application to advanced nuclear reactors, they are broadly applicable to FSI analysis of submerged components in liquid-filled vessels.

As presented in Figure 1, the reactor vessel and internal components are not concentric, prismatic, cylindrical pipes, their boundary conditions and lengths are not identical, and the vessel is not fully filled. To verify representative numerical models for the reactor of Figure 1 using the analytical solutions presented herein, the models of two concentric pipes can be developed based on the components that are pipe-type structures, including the vessel, upper internal, intermediate heat exchanger (IHX) and its shield. Examples are models for inner and outer pipes based on 1) the upper internal and the vessel, respectively, and 2) the IHX and its shield, respectively. To enable the verification, the two pipes in a model are assigned the boundary conditions, dimensions, and mechanical properties that accommodate the assumptions used for the analytical solutions. The thinnest wall thicknesses and the radii around the head support of each component (referring to h_1 , h_2 , R_1 , and R_2) and the greatest height of the two components

(referring to H) can be used for the dimensions of the two pipes in the model. The models have to be constructed using a rigid or elastic material assigned the mechanical properties of the metal used for fabricating the vessel and/or internal components (i.e., stainless steel), and use an ideal fluid with the density of the coolant (i.e., liquid sodium) at the assumed operating temperature. If the difference between the numerical and analytical results is less than or equal to $\pm 10\%$, the models should be considered to be verified.

Other analytical studies associated with submerged internal components could also be used for verification but the numerical model must reflect the assumptions made in the analytical solutions. Examples are 1) Chungand Chen (1977)²⁷, which derived frequencies of two eccentric pipes filled with fluid, used for verifying a model of the IHX and vessel of Figure 1; and 2) Chen (1975)¹¹, which derived frequencies of an array of submerged cylindrical rods, used for verifying a model for nuclear fuel rods in the coolant.

After verifying the models of submerged components (and the model of the vessel for calculating fluid-structure responses), a model including both a tank and internal components would have to be validated using data of test specimens representing the reactor of Figure 1. After verification and validation, a model could be developed for the boundary conditions, geometries, dimensions, and mechanical properties used for the reactor, accommodating the modeling approach of the verified and validated models. This model could then be used for seismic design, qualification, and risk assessment.

5. ACKNOWLEDGMENTS

The information, data, or work presented herein was funded in part by the Advanced Research Projects Agency-Energy (ARPA-E), U.S. Department of Energy, under Award Number DE-AR0000978, and in part by TerraPower, Bellevue, WA and the U.S. Department of Energy under CRADA 14CR04. The views and opinions of the authors expressed herein do not necessarily state or reflect those of the United States Government or any agency thereof, or TerraPower.

6. REFERENCES

1. Gluekler E.L. U.S. advanced liquid metal reactor (ALMR). *Prog Nucl Energy*. 1997;31(1-2):43-61.
2. Yu C.-C., Whittaker A.S. *Analytical and numerical studies of seismic fluid-structure interaction in liquid-filled vessels*, Buffalo, NY: University at Buffalo; 2020. MCEER-20-0003.
3. Jacobsen L.S. Impulsive hydrodynamics of fluid inside a cylindrical tank and of fluid surrounding a cylindrical pier. *Seismol Soc*. 1949;39(3):189-204.
4. Veletsos A. *Seismic response and design of liquid storage tanks, Guidelines for the seismic design of oil and gas pipeline systems*, Reston, VA: Committee on Gas and Liquid Fuel Lifelines, American Society of Civil Engineers (ASCE); 1984. 255-370.
5. Yu C.-C., Whittaker A.S. Analytical solutions for seismic fluid-structure interaction of head-supported cylindrical tanks. *J Eng Mech*. 2020;146(10):04020112.
6. Mir F.U.H., Yu C.-C., Whittaker A.S. Experimental and numerical studies of seismic fluid structure interaction in a base-supported cylindrical vessel. *Earthq Eng Struct Dyn*. 2020:1-19.
7. Yu C.-C., Mir F.U.H., Whittaker A.S. Validation of numerical models for seismic fluid-structure-interaction analysis of nuclear, safety-related equipment. *Nucl Eng Des*. 2021;379:1111792020.
8. Mir F.U.H., Yu C.-C., Cohen M., et al. Dataset generation for validation of fluid-structure interaction models. Paper presented at: 25th International Conference on Structural Mechanics in Reactor Technology (SMiRT-25); 2019; Charlotte, NC.
9. Mir F.U.H., Yu C.-C., Charkas H., Whittaker A.S. Validation of numerical models for seismic fluid-structure interaction analysis of advanced reactors. Paper presented at: International Congress on Advances in Nuclear Power Plants (ICAPP 2020); 2020; Abu Dhabi, United Arab Emirates.

10. Mir F.U.H., Yu C.-C., Whittaker A.S. Experiments for validation of FSI models for seismic response of advanced reactor internals. Paper presented at: 17th World Conference on Earthquake Engineering (17WCEE); 2020; Sendai, Japan.
11. Chen S. Vibration of nuclear fuel bundles. *Nucl Eng Des.* 1975;35(3):399-422.
12. Chen S. Vibrations of a row of circular cylinders in a liquid. *J Eng Ind.* 1975;97(4):1212-1218.
13. Chen S. Dynamics of heat exchanger tube banks. *J Fluids Eng.* 1977;99(3):462-467.
14. Chen S., Wambsganss M., Jendrzejczyk J. Added mass and damping of a vibrating rod in confined viscous fluids. *J Appl Mech.* 1976;43(2):325-329.
15. Chen S., Rosenberg G. Dynamics of a coupled shell-fluid system. *Nucl Eng Des.* 1975;32(3):302-310.
16. Fritz R. The effect of liquids on the dynamic motions of immersed solids. *J Eng Ind.* 1972;94(1):167-173.
17. American Society of Civil Engineers (ASCE). *Seismic analysis of safety-related nuclear structures and commentary*, Reston, VA: ASCE; 2017. ASCE/SEI 4-16.
18. Livermore Software Technology Corporation (LSTC). *LS-DYNA keyword user's manual-R11*, Livermore, CA: LSTC; 2018.
19. Flugge W. *Stresses in shells*. 1st ed., Berlin/Gottingen/Heidelberg, Germany: Springer-Verlag OHG; 1960.
20. Timoshenko S. *Vibration problems in engineering*. 1st ed., New York, NY: D. Van Nostrand Company, Inc; 1937.
21. Yu C-C, Whittaker AS. Calculations of added mass for a cylindrical component submerged in a confined fluid. 2020. <https://doi.org/10.6084/m9.figshare.13547642>.
22. Chellapandi P., Chetal S., Raj B. Application of advanced mechanics for the structural design of sodium cooled fast reactor components. *Struct Longev.* 2010;3(1-2):1-36.
23. Chellapandi P., Chetal S.C., Raj B. Investigation on buckling of FBR vessels under seismic loadings with fluid-structure interactions. *Nucl Eng Des.* 2008;238(12):3208-3217.
24. International Atomic Energy Agency (IAEA). *Status of fast reactor research and technology development*, Vienna, Austria: IAEA; 2012. IAEA-TECDOC-1691.
25. Jensen S., Ølgaard P. *Description of the prototype fast reactor at Dounreay*, Roskilde, Denmark: Rise National Laboratory; 1995. NKS/RAK-2(95)TR-C1.
26. Chopra A.K. *Dynamics of structures: theory and applications to earthquake engineering*. 4th ed., Upper Saddle River, NJ: Prentice Hall; 2012.
27. Chung H., Chen S. Vibration of a group of circular cylinders in a confined fluid. *J Appl Mech.* 1977;44(2):213-217.